Separating anisotropic and isotropic friction between atomic force microscope tips and atomically flat surfaces

Mengzhou Liao [1,*] Paolo Nicolini [1,2,†] and Tomas Polcar[1,3]

[1]*Department of Control Engineering, Faculty of Electrical Engineering, Czech Technical University in Prague, Technicka 2, 16627 Prague 6, Czech Republic*

[2]*Institute of Physics, Czech Academy of Sciences, Na Slovance 2, 182 21 Prague 8, Czech Republic*

[3]*National Centre for Advanced Tribology (nCATS), Department of Mechanical Engineering, University of Southampton, Highfield, SO17 1BJ Southampton, United Kingdom*

Layered materials are the most important class of solid lubricants. Friction on their surfaces has complex origins. Most experimental methods so far only give total friction force and cannot separate contributions from different origins. Here, we report a method to separate anisotropic and isotropic friction forces on atomically flat surfaces such as MoS_2, graphite, h-BN, and mica by combining a two-dimensional friction force microscope technology and a two-dimensional friction model. We found that the friction force of most atomically flat surfaces is anisotropic, the total force on the tip misaligns with the scan direction, and the friction anisotropy vanishes under low sliding velocity. Our two-dimensional friction model explains experimental observations. It reveals the existence of elemental hopping combinations and the isotropic component in total friction. The misalignment angle can be used to calculate the ratio of anisotropic and isotropic friction components and the ratio of resistance forces from different lattice directions. The separation of anisotropic and isotropic friction forces will offer an avenue for studying the properties of individual friction components, which can boost the study of friction mechanisms in the future and benefit the application of solid lubricants.

I. INTRODUCTION

Understanding the mechanism of friction processes is essential for reducing energy consumption. Before being known as "two-dimensional (2D) materials," layered materials like graphite, hexagonal boron nitride (h-BN), and molybdenum disulfide (MoS_2) had widely been used as solid lubricants. Layered materials have extraordinary lubricating properties because of their atomically flat surfaces and weak van der Waals (vdW) interlayer interactions, making them ideal platforms for studying the nano- to microfriction mechanism. In the past thirty years, many exciting friction phenomena like atomic "stick slip" [1], thermal effects [2–5], and superlubricity [6–9] were discovered. These phenomena are critical for bridging nano- and microfriction mechanisms.

Inherent to the nature of the crystal, layered materials show significant anisotropies in their electrical, optical, and mechanical properties [10,11]. Simulations also predicted a remarkable friction anisotropy on the surface of crystalline layered materials [12,13], but experiments poorly supported these findings [14–21]. On the one hand, the gap between simulations and experiments comes from the intrinsic limitation of the standard lateral-force atomic force microscope (LF-AFM): samples need to be rotated to measure friction forces of different crystal orientations, making it impossible

to keep the same scan area and contact in each measurement. On the other hand, friction mechanisms other than stick slip (like edge effects [9,19,22,23], chemical bonds [22,24], and adsorbates [25,26]) also play an essential role in total friction but were barely discussed. Thus, *in situ* measurements of any crystal orientation friction forces and the separation of contributions from different friction mechanisms are essential.

Here, we report a method to separate the anisotropic and isotropic friction components by combining a two-dimensional friction-force atomic force microscope (2DFF-AFM) method and a 2D friction model. In the 2DFF-AFM method, we collected the lateral force of the tip as LF-AFM and used the Z-piezo feedback signal to calculate the tip force parallel to the long direction of the cantilever [16,27]. Then, the total force at any scan angle can be calculated. We applied 2DFF-AFM measurement on several layered materials. We found that, first, the friction is anisotropic; second, the total forces misalign with scan directions; third, the friction anisotropy disappears as the scan velocity decreases. We introduced a 2D friction model to explain phenomena observed in experiments, in which we made two additional assumptions: the existence of elemental hopping combinations (EHCs) and the isotropic component in the total friction force. Our model points out that the misalignment angle provides critical information, such as the ratio of resistance forces from different EHC directions and the ratio of anisotropic and isotropic friction components in the total friction force. The separation of anisotropic and isotropic friction forces will open the door to studying the

*Corresponding author: mengzlia@fel.cvut.cz
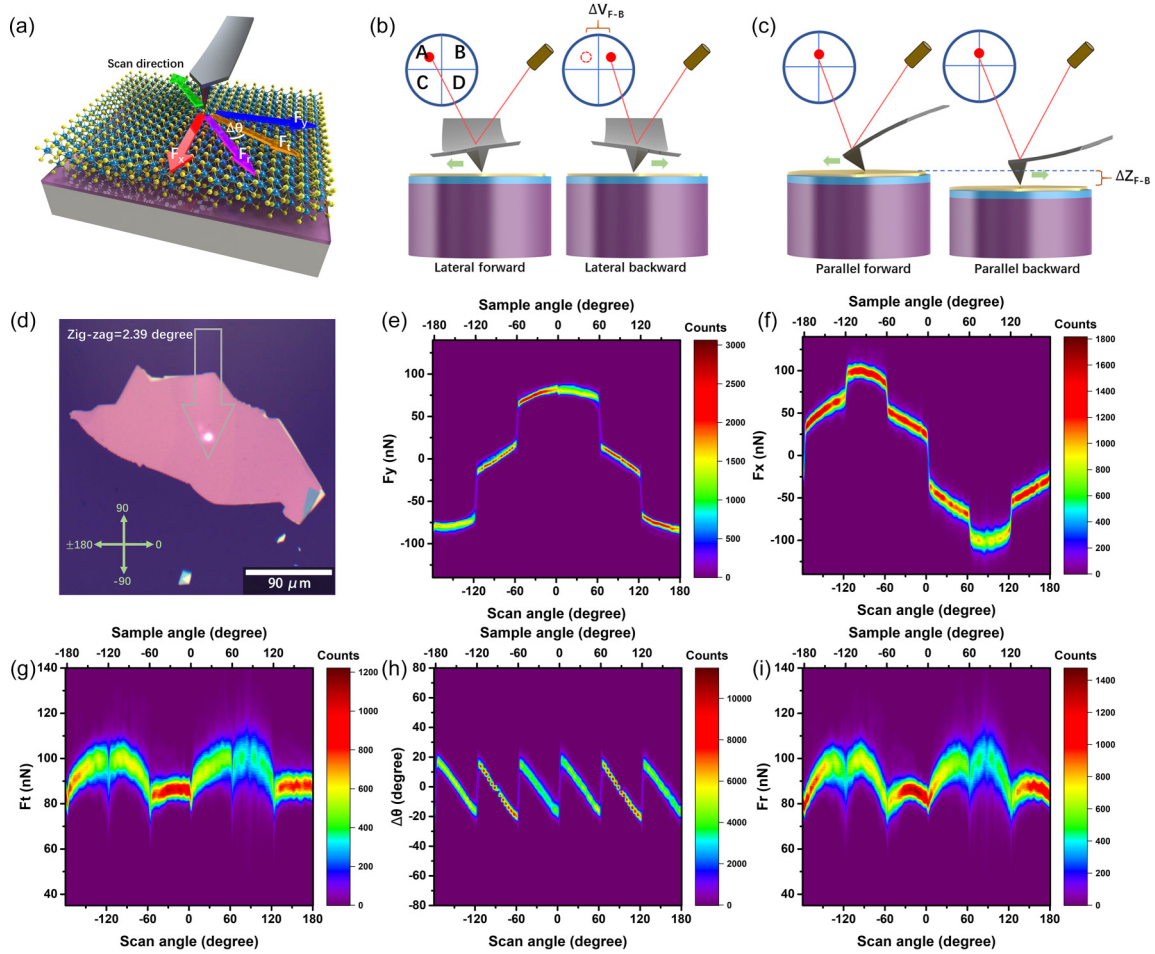
†Corresponding author: nicolini@fzu.cz

FIG. 1. Friction anisotropy of the MoS$_2$ surface. (a) Diagram of the 2DFF-AFM friction measurement. (b),(c) Diagrams depicting the measurement of the signals in the Y and X directions. (d) Image of an exfoliated MoS$_2$ flake on a Si substrate with 300-nm SiO$_2$. (e)–(i) Y-direction force (e), X-direction force (f), total force (g), misalignment angle (h), and friction force (i) as a function of the scan and sample angles.

property of individual components, which is critical for further revealing the friction mechanisms in solid lubricants.

II. EXPERIMENTAL RESULTS OF FRICTION ANISOTROPY ON MULTIPLE ATOMICALLY FLAT SURFACES

A. 2DFF-AFM method

As shown in Fig. 1(a), the sample is fixed in our 2DFF-AFM method, and we change scan directions to measure the friction properties of different lattice orientations. Here we define the force perpendicular to the long direction of the cantilever as F_y and the force along the long direction of the cantilever as F_x. As shown in Fig. 1(b), F_y can be calculated in the same way as the standard LF-AFM method: $2F_y = k_y(V_{(A+C)-(B+D)}^{\text{Forward}} - V_{(A+C)-(B+D)}^{\text{Backward}}) = k_y \Delta V_{F-B}$, where $V_{(A+B)-(C+D)}$ is the lateral torsion signal of the cantilever and k_y is the lateral sensitivity parameter. For F_x, when the force on the AFM tip is parallel to the long direction of the cantilever, as shown in Fig. 1(c), there is an extra vertical bending. The function of Z feedback control is to keep the vertical bending signal $V_{(A+B)-(C+D)}$ constant (which is the set point). Thus, the Z piezo will move for a distance

$\Delta Z_{F-B} = Z_{\text{Forward}} - Z_{\text{Backward}}$ to cancel the extra bending signal caused by F_x, so that $2F_x = k_x \Delta Z_{F-B}$, where k_x is the X-direction sensitivity parameter. With known F_x and F_y, we can then calculate the value and angle of the total force F_t, and the misalignment angle $\Delta\theta$ between the total force and the scan direction. The friction force is calculated as $F_r = F_t \cos \Delta\theta$. In Fig. S4 of the Supplemental Material [28], we used the 2DFF-AFM method to measure an amorphous SiO$_2$ surface with a silicon tip, which demonstrates the validity of the 2DFF-AFM method. For more details on the 2DFF-AFM method, please refer to Supplemental Material Note 1 [28].

B. Friction properties of atomically flat surfaces

We used the 2DFF-AFM method to measure the friction anisotropy properties of different exfoliated layered materials, including MoS$_2$, graphite, h-BN, and mica. Figure 1(d) shows the microscope image of the exfoliated MoS$_2$ flake on the silicon substrate with a 300-nm SiO$_2$ oxidation layer. The tip position and coordinate axes are marked in the image. The thickness of the MoS$_2$ flake in Fig. 1(d) is about 47.66 nm (Fig. S7 [28]). We used the sharp edges of the MoS$_2$ flakes to determine the zigzag direction [29] and defined one of
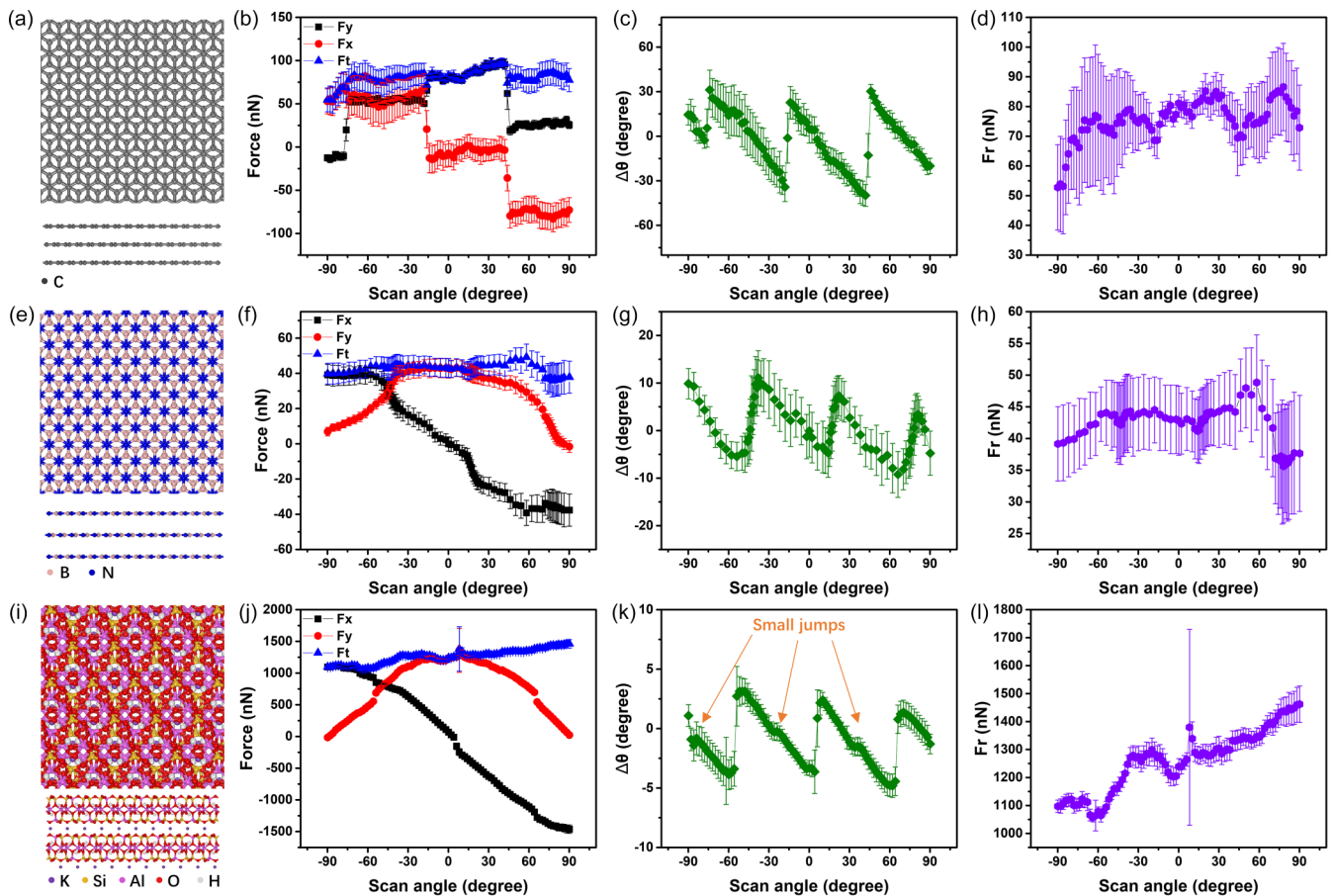
FIG. 2. Friction anisotropy of other 2D surfaces: graphite, h-BN and mica. (a) Top and side view of the graphite structure. (b)–(d) Friction anisotropy results between the silicon tip and the graphite surface: x, y directions and total force (b), misalignment angle (c), and friction force (d) as a function of the scan angle. (e) Top and side views of the h-BN structure. (f)–(h) Friction anisotropy results between the silicon tip and the h-BN surface: x, y directions and total force (f), misalignment angle (g), and friction force (h) as a function of the scan angle. (i) Top and side views of the mica structure. (j)–(l) Friction anisotropy results between the silicon tip and the mica surface: x, y directions and total force (j), misalignment angle (k), and friction force (l) as a function of the scan angle.

the zigzag directions as the zero degree of the sample angle. For more details on the sample preparation, please refer to Supplemental Material Note 2.

Figures 1(e)–1(i) show typical friction properties of the MoS_2 surface. We used a standard contact mode silicon tip ARROW-CONTR(NANO WORLD) to perform the measurement with a normal load of 216.83 nN and a scan velocity of 60 μm/s under ambient conditions. Unlike the isotropic amorphous SiO_2 surface, Figs. 1(e) and 1(f) show that F_y and F_x change discontinuously with the scan angle. Sudden jumps happen in zigzag directions. Figure 1(g) shows that the total force F_t has a periodic structure combining 60° and 180° period signals. In Fig. 1(h), the direction of F_t misaligns with the scan direction, and the misalignment angle $\Delta\theta$ presents a sawtooth shape with sudden jumps in zigzag directions. The period of $\Delta\theta$ is 60°, and its amplitude is about 20°. The friction force F_r in Fig. 1(i) shows that the zigzag and armchair directions have the lowest and highest friction forces, respectively. We also notice that F_r has two components with 60° and 180° periodicities. In Fig. S9, we repeated the same measurement after rotating the MoS_2 sample through by about 33°. After the rotation, F_x, F_y, $\Delta\theta$, and the 60° period signals

in F_t and F_r shift with the rotating angle, but the 180° period signals in F_t and F_r remain the same.

We also used a stiffer silicon tip 240AC-NA (OPUS), a 150-nm diamondlike carbon tip NT B150 (Nanotools), and a 2-μm SiO_2 ball tip CP-CONT-SiO (NANOSENSORS) to perform the 2DFF-AFM measurements on the MoS_2 surface (see Figs. S10–S12). Results from these tips are similar to the standard silicon tip (Fig. 1), which means that the tip material, the cantilever stiffness, and the contact area will not play a decisive role in the friction anisotropy of atomically flat surfaces. However, there are still some differences: first, in Fig. S10, the 180° period signals in F_t and F_r vanish when measured by the stiffer silicon tip 240AC-NA (OPUS); second, the amplitudes of $\Delta\theta$ in each measurement are different. For more details, please refer to Supplemental Material Note 3.

We also performed 2DFF-AFM measurements on other layered materials: graphite, h-BN, and mica with the same silicon tip and scan parameters as in Fig. 1. In Fig. 2, we show only scan angles as the sharp edges cannot be used to determine the crystal orientation [29] for these layered materials. As shown in Figs. 2(a)–2(d), results from graphite show distinct friction anisotropy properties.
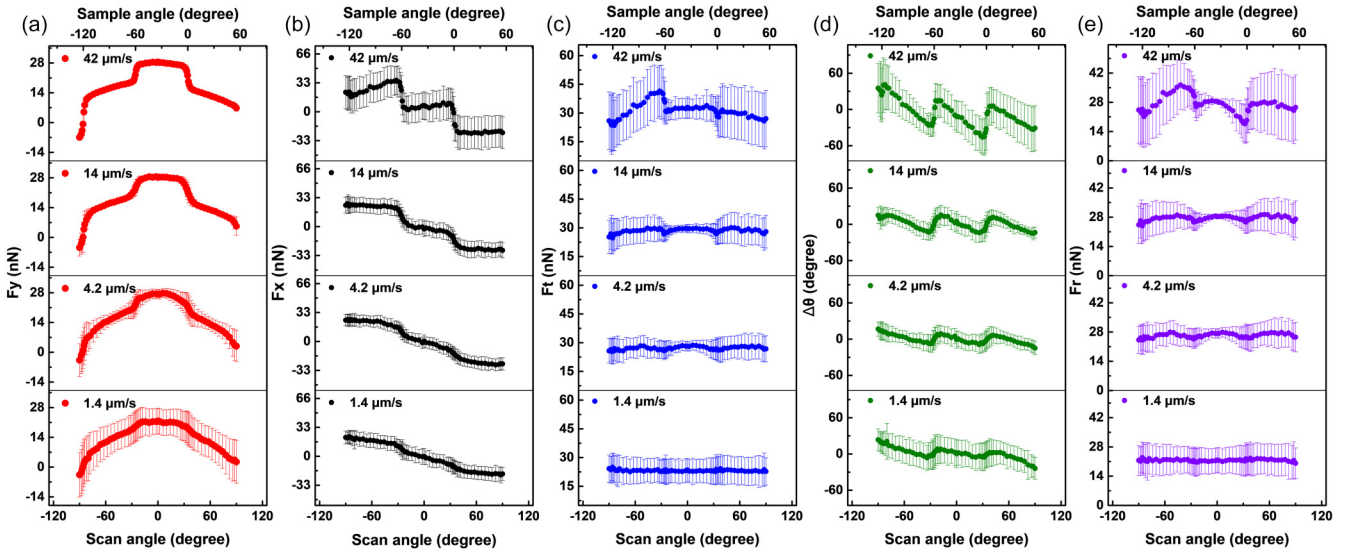
FIG. 3. The evolution of the friction anisotropy on the bulk MoS$_2$ surface with different sliding velocities. (a)–(e) Y-direction force (a), X-direction force (b), total force (c), misalignment angle (d), and friction force (e) as a function of the scan and sample angles with different sliding velocities. The normal load is set to 216.83 nN.

In Fig. 2(c), the period and amplitude of $\Delta\theta$ are about 60° and 30°, respectively. Figures 2(e)–2(h) show that the friction anisotropy of the h-BN surface is much weaker than the MoS$_2$ and graphite surfaces. From Fig. 2(f), we can see that the jumps in F_y and F_x are not so obvious. In Fig. 2(g), the period of $\Delta\theta$ is still 60°, but the amplitude is just 10°. In Fig. 2(h), the 60° period signal in F_r of the h-BN surface is unobvious. As shown in Figs. 2(i)–2(l), the mica surface shows a nearly isotropic friction behavior consistent with the previous report [30]. There are still small jumps in Fig. 2(j), however, F_t and F_r [Fig. 2(l)] are without any visible periodic pattern. Although friction anisotropy has vanished on the mica surface, we can still observe a distinct pattern in $\Delta\theta$ with a 60° period and about 3° amplitude [Fig. 2(k)]. Unlike the other layered materials presented earlier, mica has small jumps (of about 0.4°) in $\Delta\theta$ at the middle of each 60° period. In Figs. 2(b), 2(d), 2(f), 2(h), 2(j), and 2(l), the measured forces are monotonously drifting mainly due to the thermal effect. For more detailed discussions about the monotonous drifts of forces, please refer to Supplemental Material Note 1.

C. Effect of the scan velocity and the load

We performed 2DFF-AFM measurements on the MoS$_2$ surface with different normal loads and scan velocities. As shown in Fig. S13, most friction properties do not change significantly even when the normal load ranges from positive to negative. Only the 180° period signals in F_t and F_r are different. Our results indicate that the normal load (pressure) does not strongly influence friction anisotropy properties. However, as shown in Fig. 3, when we fix the normal load at 216.83 nN, the level of friction anisotropy of the MoS$_2$ surface monotonously decreases as the scan velocity reduces. The friction of the MoS$_2$ surface becomes near isotropic when the scan velocity is 1.4 μm/s.

III. THEORETICAL EXPLANATION AND DISCUSSION

A. A two-dimensional friction model

Here we introduce a 2D friction model with thermal effects to explain the friction anisotropy phenomena on atomically flat surfaces. Our model has two basic assumptions: the existence of elemental hopping combinations (EHCs) and isotropic components in the total friction force.

Following the approach exploited in the 2D Prandtl-Tomlinson model [13,31], we assume that the interaction between tip and substrate can be described by an effective potential energy surface (PES) and an elemental hopping mode (EHM) is represented by a path that connects two neighboring minima in the PES. For the example reported in Fig. 4(a), there is one global (marked with "1") and one local (marked with "2") minimum in the unit cell (highlighted with the gray dashed line). Consequently, there are two possible independent EHMs: $1 \to 2$ and $2 \to 1$. Considering the hexagonal symmetry of the example in Fig. 4(a), two possible combinations can be chosen: (i) the path $1 \to 2 \to 1^{I} \to \to 2^{I} \to 1^{III}$, which we call nonidentical combinations (in white); and (ii) the path $1 \to 2 \to 1^{II} \to 2^{II} \to 1^{IV}$, termed identical combinations (in red). The directions identified by these two paths are referred to as elemental hopping combinations (EHCs), and any sliding motion between global minima can then be decomposed into a sequence of EHCs. Moreover, the direction of an EHC always aligns with a crystal orientation and has a particular barrier. Thus, sliding along different EHC directions can offer different sliding resistances, and the total resistance force for an arbitrary sliding direction can be considered as the resultant resistance forces from all EHC directions.

The isotropic component in total friction force can originate from mechanisms that the Prandtl-Tomlinson model cannot describe, such as the edge pinning effect, chemical bonds [9,24], contamination [25], etc. We assume these kinds
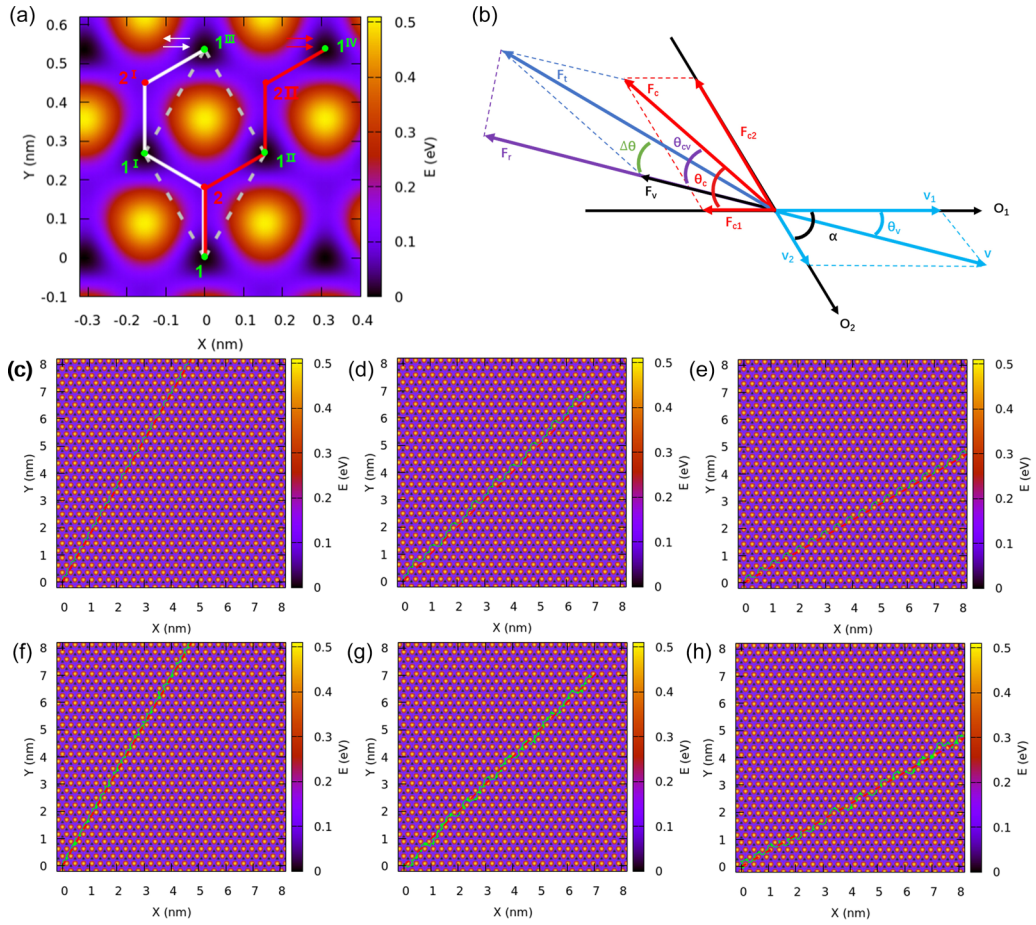
FIG. 4. Diagrams of EHCs. (a) Potential energy surface of an amorphous SiO_2 slab interacting with a MoS_2 layer. (b) Diagram illustrating the 2D sliding model with two EHCs. (c)–(e) The trajectory of the PT particle with $T = 0$ K, $k = 1$ N/m, $v = 2000$ nm/s, and in the critical damping regime. Trajectories followed by the PT particle when sliding along (c) $0°$ (zigzag direction), (d) $15°$, and (e) $30°$ (armchair direction). (f)–(h) The trajectory of the PT particle with $T = 300$ K, $k = 1$ N/m, $v = 2000$ nm/s, and in the critical damping regime. Trajectories followed by the PT particle when sliding along (f) $0°$ (zigzag direction), (g) $15°$, and (h) $30°$ (armchair direction).

of friction will not change with the sliding direction. For a more detailed discussion of the origins of isotropic and anisotropic friction components, please refer to Supplemental Material Note 8.

Figure 4(b) shows a simple diagram of the 2D surface with two EHCs: O_1 and O_2, with an angle of α between them. Consider a tip sliding with velocity v; the velocity components along the O_1 and O_2 directions (v_1 and v_2) are then

$$v_1 = v \frac{\sin(\alpha - \theta_v)}{\sin \alpha}; \quad v_2 = v \frac{\sin \theta_v}{\sin \alpha}, \tag{1}$$

where θ_v is the angle between the sliding direction and O_1. The total force F_t can be decomposed into an isotropic component F_v (aligned along the sliding direction) and an anisotropic one F_c (which originates from the EHCs). The F_c can be projected onto the O_1 and O_2 directions, identifying the vectors F_{c1} and F_{c2}, then

$$\frac{\sin\theta_c}{\sin(\alpha - \theta_c)} = \frac{F_{c2}}{F_{c1}} = G, \tag{2}$$

where θ_c is the angle between F_c and O_1, where

$$\theta_c = \tan^{-1}\left(\frac{G \sin \alpha}{1 + G \cos \alpha}\right) \tag{3}$$

Let us define

$$\theta_{cv} = \theta_c - \theta_v \tag{4}$$

then

$$\frac{\sin \Delta\theta}{\sin(\theta_{cv} - \Delta\theta)} = \frac{F_c}{F_v} = P \tag{5}$$

with $\Delta\theta$ being the misalignment angle between the scan direction and the total force. So

$$\Delta\theta = \tan^{-1}\left(\frac{P \sin \theta_{cv}}{1 + P \cos \theta_{cv}}\right). \tag{6}$$

The friction force F_r is

$$F_r = F_t \cos \Delta\theta. \tag{7}$$

Notice that the direction of EHC is periodical because of the lattice symmetry. Thus, O_1 and O_2 will switch directions for each period, leading to jumps in F_x and F_y at $n\alpha$ (n is an integer) sliding angles.

With thermal effects taking place during sliding, previous works [4,5] provided an expression of the mean friction force

F_{ci} along an elemental hopping direction O_i as follows:

$$\frac{1}{\beta_i k_B T}(F_i^* - F_{ci})^{3/2} = \ln\frac{v_{0_i}}{v_i} - \frac{1}{2}\ln\left(1 - \frac{F_{ci}}{F_i^*}\right), \quad (8)$$

where k_B is the Boltzmann constant, T is the temperature, and F_i^* is the mean friction force along the O_i direction at 0 K. Equation (8) has been derived following a master equation approach for the sliding in the one-dimensional case. Here we make the implicit assumption that this relation holds for elemental hopping combinations as well, and even if the elemental hopping modes are not strictly 1D. The v_{0_i}, β_i, and critical frequency f_{0_i} are related via

$$v_{0_i} = \frac{2 f_{0_i}\beta_i k_B T}{3 k_{\text{series}_i}\sqrt{F_i^*}}, \quad (9)$$

with k_{series_i} being the effective stiffness of the contact along the EHC direction. From these equations, one can see that the friction anisotropy phenomenon naturally originates from the existence of EHCs.

We used two-dimensional Prandtl-Tomlinson (2D PT) simulations to support our assumptions of EHCs. Figures 4(c)–4(e) show the trajectory followed by the PT particle at $T = 0$ K, superimposed onto the PES map. Figures 4(c) and 4(e) show that when sliding along the zigzag (0°) and armchair directions (30°), the sliding motion of the particle consists solely of identical and nonidentical hoppings, respectively. For the 15° sliding direction, the route is a 1:1 combination of identical and nonidentical hoppings [Fig. 4(d)], supporting our assumption. For the temperature > 0 K, the hopping will not be limited from one minimum to another due to thermal effects. As shown in Fig. S19, the hopping of the point contact becomes random at 300 K for low sliding velocities, which implies the vanishing of the anisotropic friction. However, when increasing the sliding velocity, the level of the random hopping monotonously decreases. As shown in Figs. 4(f)–4(h), the motion fully follows minimum-to-minimum paths when the sliding velocity is > 2000 nm/s. The 2D PT simulation results support our assumptions about the role played by elemental hopping combinations. Please refer to Supplemental Material Note 7 for more details and discussion about the model.

B. Discussion of the 0-K condition

For the 0-K condition, F_{c1} and F_{c2} are constant for all velocities as the thermal effects vanish:

$$F_{c1} = \begin{cases} F_1^* & \theta_v \neq (2n+1)\alpha \\ 0 & \theta_v = (2n+1)\alpha \end{cases}, \quad F_{c2} = \begin{cases} F_2^* & \theta_v \neq 2n\alpha \\ 0 & \theta_v = 2n\alpha \end{cases},$$

with n being an integer number. In the simplest case, $F_v = 0$ and $F_t = F_c$. $\Delta\theta$ and F_r only change with the ratio F_2^*/F_1^*. In Fig. 5(a$_1$), the period of the misalignment angle is 2α, and there is a "jump" at $\theta_v = \alpha$. When the ratio F_2^*/F_1^* grows, the amplitude of $\Delta\theta$ monotonically increases from α to 2α, and the scale of the jump at $\theta_v = \alpha$ monotonically decreases from α to 0. In Fig. 5(a$_2$), the amplitude of the friction force ($\theta_v \neq n\alpha$) increases with the F_2^*/F_1^* ratio. When fixing F_2^*/F_1^* to 10 and increasing F_v, the isotropic friction force F_v can eliminate friction anisotropy. As shown in

Figs. 5(b$_1$)–5(b$_3$), the total force changes with F_v, the amplitude and the scale of jump at $\theta_v = \alpha$ of the misalignment angle monotonically decreases as F_v increases, and the friction force variation vanishes as F_v increases.

C. Discussion of the $T > 0$ K condition

Thermal effects need to be considered for finite temperatures. According to Eq. (11),

$$v_i = v_{0_i}\left(1 - \frac{F_{ci}}{F_i^*}\right)^{-1/2} e^{-(F_i^* - F_{ci})^{3/2}/\beta_i k_B T}. \quad (10)$$

Two critical velocities v_{TLi} and v_{TMi} can be identified. For v_{TLi}, when $v_i \leqslant v_{TLi}$, $F_{ci} = 0$. So

$$v_{TLi} = v_{0_i} e^{-(F_i^*)^{3/2}/\beta_i k_B T} \quad (11)$$

v_{TMi} is the critical velocity at which friction saturates $F_{ci} \approx F_i^*$. Then we can set

$$v_{TMi} = \frac{v_{0_i}}{\sqrt{1-m}} e^{-[F_i^*(1-m)]^{3/2}/\beta_i k_B T}, \quad (12)$$

where $m = \frac{F_{ci}}{F_i^*}$, and in the following, we choose $m = 0.99$. The relation between the scan velocity v and v_{TMi}, v_{TLi} determines the friction properties of each direction of the EHC.

In Fig. 5(c), we set $F_2^* = 10 F_1^*$, and $F_{c2} > F_{c1}$. We divide it into five regions: region I: $v_i \leqslant v_{TL2}$, $F_{c1} = F_{c2} = 0$; region II: $v_{TL2} < v_i \leqslant v_{TL1}$, $F_{c1} = 0$, F_{c2} increases logarithmically with the velocity; region III: $v_{TL1} < v_i \leqslant v_{TM1}$, F_{c1} and F_{c2} both increase logarithmically with the velocity; region IV: $v_{TM1} < v_i \leqslant v_{TM2}$, $F_{c1} \approx F_1^*$, F_{c2} increases logarithmically with the velocity; and region V: $v_i > v_{TM1}$, $F_{c1} \approx F_1^*$, $F_{c2} \approx F_2^*$. We first discuss the simplest case with the isotropic force $F_v = 0$. For $v < v_{TL2}$, v_1 and v_2 are in region I for all sliding angles, the sliding is frictionless. For $v_{TL2} < v < v_{TL1}$, only F_{c2} provides a friction force for all sliding angles, similar to the identical O_1 and O_2 conditions (see Fig. S15). When $v > v_{TL1}$, both EHC directions contribute to friction. As shown in Figs. 5(d$_1$)–5(d$_3$), we use $v = v_{TM1}$, v_{TM2}, $10 v_{TM2}$, and $400 v_{TM2}$, where v_1 and v_2 are primarily in regions III, IV, V, and V (ultrahigh velocity), respectively, as examples to show the influences of the sliding velocity. In Fig. 5(d$_1$), the amplitude of total force increases monotonously with the sliding velocity. In Fig. 5(d$_2$), velocity does not change the amplitude of the misalignment angle significantly, but the jump at $\theta_v = \alpha$ increases with velocity. In Fig. 5(d$_3$), the amplitude of friction force increases monotonously with the sliding velocity.

Generally, the friction anisotropy properties evolve towards the 0 K condition as the velocity increases. However, the level of friction anisotropy does not increase monotonically with the velocity. When $v < v_{TM2}$, the amplitudes of total and friction forces increase with sliding velocity, intensifying the friction anisotropy. When $v > v_{TM2}$, both F_{c1} and F_{c2} reach plateaus, and further increasing the velocity will sharper the variations of total and friction force near the O_1 or O_2 directions. When transition regions near the O_1 or O_2 directions become small enough, friction variation cannot be experimentally detected by the device due to the limited resolution, which explains why superlubric directions are predicted in previous simulations but not yet found in experiment [31,32].
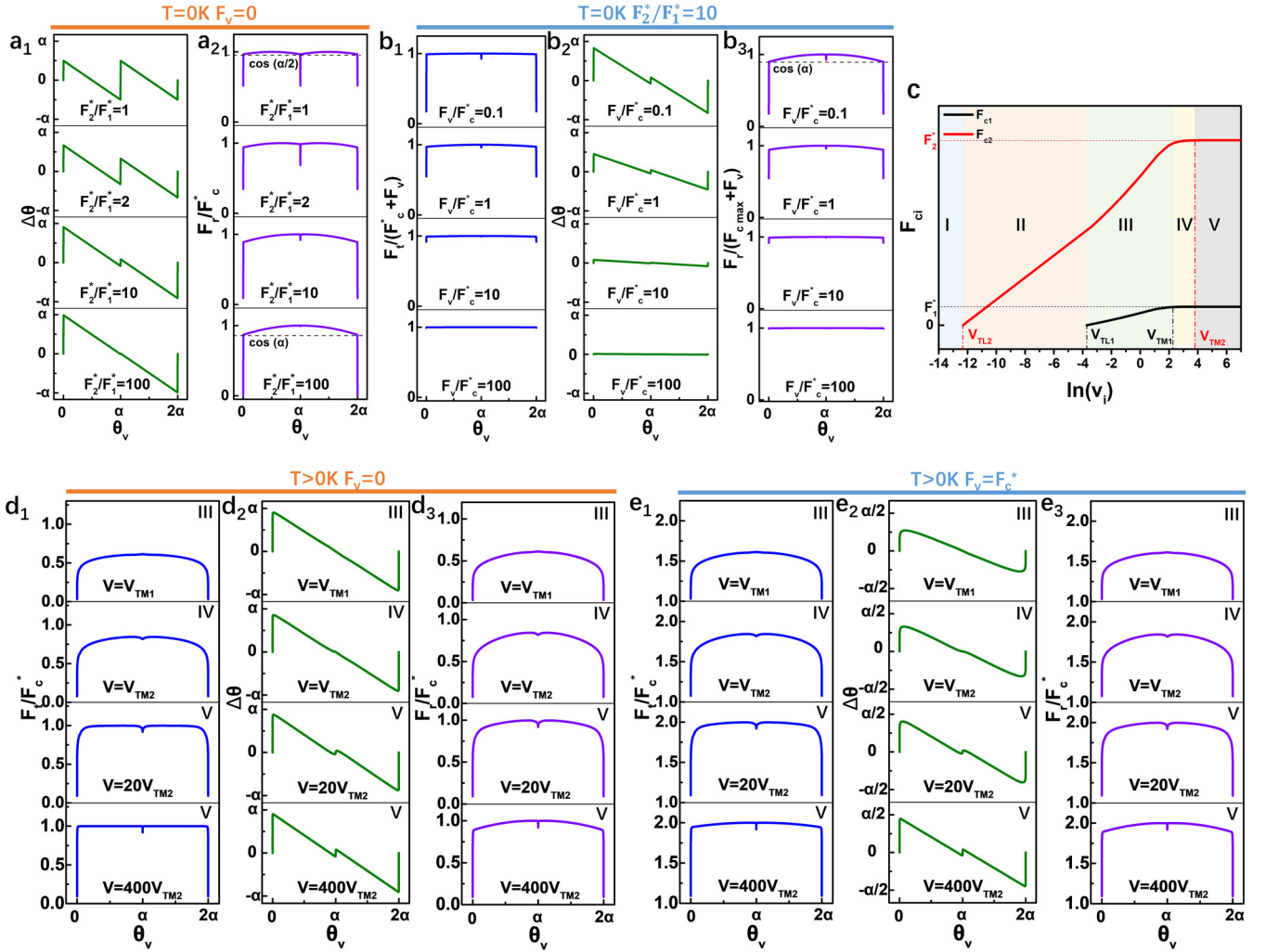
FIG. 5. Theoretical calculations of friction on an atomically flat surface with two EHCs. (a$_1$),(a$_2$) Misalignment angle (a$_1$) and normalized friction force (a$_2$) as a function of the sliding angle at $T = 0$ K with $F_v = 0$ and different F_2^*/F_1^* ratios, $F_c^* = F_2^* \frac{\sin\alpha}{\sin\theta_c}$ ($\theta_v \neq n\alpha$). (b$_1$)–(b$_3$) Normalized total force (b$_1$), misalignment angle (b$_2$), and normalized friction force (b$_3$) as a function of the sliding angle at $T = 0$ K with $F_2^*/F_1^* = 10$ and different F_v, $F_{c\,max} = F_2^* \frac{\sin\alpha}{\sin\theta_c}$. (c) An example of F_{c1} and F_{c2} as functions of $\ln(v_i)$ for $T > 0$ K; parameters come from Ref. [4]. (d$_1$)–(d$_3$) Normalized total force (d$_1$), misalignment angle (d$_2$), and normalized friction force (d$_3$) as functions of sliding angles at different sliding velocities with $F_v = 0$; F_{c1} and F_{c2} are from (c). (e$_1$)–(e$_3$) Normalized total force (e$_1$), misalignment angle (e$_2$), and normalized friction force (e$_3$) as functions of sliding angles at different sliding velocities, with $F_v = F_c^*$; F_{c1} and F_{c2} are from (c).

Now we consider the condition with isotropic friction force $F_v = F_c^*$. When $v < v_{TL2}$, then $F_{c1} = F_{c2} = 0$ and $F_t = F_r = F_v$, the friction is isotropic. When $v_{TL2} < v < v_{TL1}$, then only F_{c1} provides friction force, and it can be considered the same as identical O$_1$ and O$_2$ with $F_v = F_c^*$ (see Fig. S15). As shown in Figs. 5(e$_1$)–5(e$_3$), compared with the condition with $F_v = 0$, when $v > v_{TL1}$, first, the amplitudes of F_t and F_r are the same, but the ratio between maxima and minima decreases. Second, the amplitude of $\Delta\theta$ is smaller and decreases as velocity reduces. Therefore, friction anisotropy will vanish with a nonzero isotropic friction force as the sliding velocity decreases, which perfectly fits our observations in Fig. 3.

IV. CALCULATION OF THE ISOTROPIC AND ANISOTROPIC FRICTION FORCE COMPONENTS

Figure 5 shows that thermal effects are negligible for a high enough scan velocity. Considering two EHCs with $F_{c2} > F_{c1}$,

according to Eqs. (2)–(6), the amplitude of $\Delta\theta$ is

$$\Delta\theta_{max} = \tan^{-1}\left(\frac{P\sin\theta_c}{1 + P\cos\theta_c}\right) \qquad (13)$$

and the scale of the jump at $\theta_v = \alpha$ is

$$\Delta\theta_{jump} = 2\tan^{-1}\left(\frac{P\sin(\alpha - \theta_c)}{1 + P\cos(\alpha - \theta_c)}\right). \qquad (14)$$

Thus, we can get the ratio between isotropic and anisotropic friction force P and the ratio of the maximum friction forces along the EHCs G by measuring the amplitude and the scale of jumps in $\Delta\theta$. In Fig. 1(h), no jump is observed, and the amplitude is about 20°. We can conclude that on the MoS$_2$ surface, the friction force along the zigzag direction is negligible compared to the armchair direction, which agrees with the simulation results [31], and the ratio between isotropic and anisotropic friction force P is about 0.5. In Fig. 2, the graphite and h-BN surfaces both have

no jumps in $\Delta\theta$, which means one EHC direction (most likely zigzag direction) has much higher sliding resistance than the other. For graphite, the 30° amplitude of $\Delta\theta$ shows that the isotropic friction is negligible. For h-BN, the amplitude is about 10°, and therefore P is about 2, indicating that the friction on the h-BN surface is contributed mainly by isotropic components. The results from the mica surface are complex: the profile of $\Delta\theta$ has around 3° amplitude and a 0.4° jump. Then, G and P are about 13.0 and 8.1 for mica, respectively, which means both EHCs on mica contribute to friction, and isotropic friction dominates the friction process.

V. CONCLUSION

Our work continues and extends the previous experimental and theoretical efforts [13,16,27,30,33,34] by introducing a 2DFF-AFM method and a two-dimensional friction model critical for characterizing the friction properties of atomically flat surfaces over a range of contact conditions. Overall, our results indicate that the friction anisotropy phenomenon is complex and influenced by environmental and scan parameters. We observed distinctive effects on the profiles of the friction force and the total force acting on the AFM tip. The experimental results motivated us to introduce a separation between anisotropic and isotropic components of the friction force, which depend differently on the sliding speed and direction. Based on these definitions, we developed a minimalistic model by introducing a few more assumptions, e.g., the presence of a limited set of elemental hopping combinations—EHCs, which successfully explains the experimental findings. In addition, the misalignment angle between total and friction forces turned out to be a robust quantity to characterize anisotropy, allowing us to calculate the ratio of friction forces at different EHCs, and the contributions from anisotropic and isotropic friction forces. The gradual reduction of the anisotropy degree at increasing velocities suggests that the friction mechanism dominating the friction process could be different at high and low velocities due to the existing isotropic friction force and thermal effects. The separation into anisotropic and isotropic friction forces makes it possible to study further the origin of isotropic friction, which is critical for deepening our knowledge of the friction mechanisms in solid lubricants under environmental control. Sliding along the EHCs directions with low sliding resistance and eliminating the isotropic friction with surface treatments could be an efficient way to significantly reduce the friction of layered materials, potentially enhancing the performance of solid lubricants.

VI. METHODS

Sample preparation. In this experiment, the MoS_2, graphite, and h-BN samples were produced by mechanically exfoliating Synthetic Molybdenum Disulfide (2Dsemiconductors), Graphenium graphite (Manchester Nanomaterials), and h-BN crystals (2Dsemiconductors), respectively. The substrate is silicon with 300-nm SiO_2.

Sample characterizations. AFM measurements were performed on a WITec alpha300 RAS. We used theoretical calculation to calibrate the cantilever in the vertical direction (please refer to Supplemental Material Note 1 for more details). PL and Raman characterizations were performed on a Horiba XploRA^{TM} PLUS Raman system. The laser wavelength was 532 nm.

---

[1] C. M. Mate, G. M. McClelland, R. Erlandsson, and S. Chiang, Atomic-Scale Friction of a Tungsten Tip on a Graphite Surface, Phys. Rev. Lett. **59**, 1942 (1987).

[2] E. Gnecco, R. Bennewitz, T. Gyalog, C. Loppacher, M. Bammerlin, E. Meyer, and H. J. Güntherodt, Velocity Dependence of Atomic Friction, Phys. Rev. Lett. **84**, 1172 (2000).

[3] Y. Sang, M. Dubé, and M. Grant, Thermal Effects on Atomic Friction, Phys. Rev. Lett. **87**, 174301 (2001).

[4] E. Riedo, E. Gnecco, R. Bennewitz, E. Meyer, and H. Brune, Interaction Potential and Hopping Dynamics Governing Sliding Friction, Phys. Rev. Lett. **91**, 084502 (2003).

[5] Q. Li, Y. Dong, D. Perez, A. Martini, and R. W. Carpick, Speed Dependence of Atomic Stick-Slip Friction in Optimally Matched Experiments and Molecular Dynamics Simulations, Phys. Rev. Lett. **106**, 126101 (2011).

[6] M. Dienwiebel, G. S. Verhoeven, N. Pradeep, J. W. M. Frenken, J. A. Heimberg, and H. W. Zandbergen, Superlubricity of Graphite, Phys. Rev. Lett. **92**, 126101 (2004).

[7] H. Li, J. Wang, S. Gao, Q. Chen, L. Peng, K. Liu, and X. Wei, Superlubricity between MoS_2 monolayers, Adv. Mater. **29**, 1701474 (2017).

[8] Y. Song, D. Mandelli, O. Hod, M. Urbakh, M. Ma, and Q. Zheng, Robust microscale superlubricity in graphite/hexagonal boron nitride layered heterojunctions, Nat. Mater. **17**, 894 (2018).

[9] M. Liao, P. Nicolini, L. Du, J. Yuan, S. Wang, H. Yu, J. Tang, P. Cheng, K. Watanabe, T. Taniguchi, L. Gu, V. E. P. Claerbout, A. Silva, D. Kramer, T. Polcar, R. Yang, D. Shi, and G. Zhang, Ultra-low friction and edge-pinning effect in large-lattice-mismatch van der Waals heterostructures, Nat. Mater. **21**, 47 (2022).

[10] C. Gong, Y. Zhang, W. Chen, J. Chu, T. Lei, J. Pu, L. Dai, C. Wu, Y. Cheng, T. Zhai, L. Li, and J. Xiong, Electronic and optoelectronic applications based on 2D novel anisotropic transition metal dichalcogenides, Adv. Sci. **4**, 1700231 (2017).

[11] L. Du, T. Hasan, A. Castellanos-Gomez, G.-B. Liu, Y. Yao, C. N. Lau, and Z. Sun, Engineering symmetry breaking in 2D layered materials, Nat. Rev. Phys. **3**, 193 (2021).

[12] O. Y. Fajardo, E. Gnecco, and J. J. Mazo, Anisotropy effects and friction maps in the framework of the 2d PT model, Phys. B (Amsterdam, Neth.) **455**, 44 (2014).

[13] E. Gnecco, O. Y. Fajardo, C. M. Pina, and J. J. Mazo, Anisotropy effects in atomic-scale friction, Tribol. Lett. **48**, 33 (2012).

[14] J. S. Choi, J. S. Kim, I. S. Byun, D. H. Lee, M. J. Lee, B. H. Park, C. Lee, D. Yoon, H. Cheong, K. H. Lee, Y. W. Son, J. Y. Park, and M. Salmeron, Friction anisotropy-driven domain imaging on exfoliated monolayer graphene, Science **333**, 607 (2011).

[15] K. Miura, N. Sasaki, and S. Kamiya, Friction mechanisms of graphite from a single-atomic tip to a large-area flake tip, Phys. Rev. B **69**, 075420 (2004).

[16] S. G. Balakrishna, A. S. De Wijn, and R. Bennewitz, Preferential sliding directions on graphite, Phys. Rev. B **89**, 245440 (2014).

[17] C. M. Almeida, R. Prioli, B. Fragneaud, L. G. Cançado, R. Paupitz, D. S. Galvão, M. De Cicco, M. G. Menezes, C. A. Achete, and R. B. Capaz, Giant and tunable anisotropy of nanoscale friction in graphene, Sci. Rep. **6**, 31569 (2016).

[18] M. R. Vazirisereshk, K. Hasz, R. W. Carpick, and A. Martini, Friction anisotropy of MoS_2: effect of tip–sample contact quality, J. Phys. Chem. Lett. **11**, 6900 (2020).

[19] C. Lee, Q. Li, W. Kalb, X.-Z. Liu, H. Berger, R. W. Carpick, and J. Hone, Frictional characteristics of atomically thin sheets, Science **328**, 76 (2010).

[20] Y. Song, J. Wang, Y. Wang, M. Urbakh, Q. Zheng, and M. Ma, Directional anisotropy of friction in microscale superlubric graphite/*h*BN heterojunctions, Phys. Rev. Mater. **5**, 084002 (2021).

[21] K. Xu, Y. Pan, S. Ye, L. Lei, S. Hussain, Q. Wang, Z. Yang, X. Liu, W. Ji, R. Xu, and Z. Cheng, Shear anisotropy-driven crystallographic orientation imaging in flexible hexagonal two-dimensional atomic crystals, Appl. Phys. Lett. **115**, 063101 (2019).

[22] Z. Deng, A. Smolyanitsky, Q. Li, X.-Q. Feng, and R. J. Cannara, Adhesion-dependent negative friction coefficient on chemically modified graphite at the nanoscale, Nat. Mater. **11**, 1032 (2012).

[23] S. Li, Q. Li, R. W. Carpick, P. Gumbsch, X. Z. Liu, X. Ding, J. Sun, and J. Li, The evolving quality of frictional contact with graphene, Nature (London) **539**, 541 (2016).

[24] K. Tian, N. N. Gosvami, D. L. Goldsby, Y. Liu, I. Szlufarska, and R. W. Carpick, Load and Time Dependence of Interfacial Chemical Bond-Induced Friction at the Nanoscale, Phys. Rev. Lett. **118**, 076103 (2017).

[25] A. Pálinkás, G. Kálvin, P. Vancsó, K. Kandrai, M. Szendrö, G. Németh, M. Németh, Á. Pekker, J. S. Pap, P. Petrik, K. Kamarás, L. Tapasztó, and P. Nemes-Incze, The composition and structure of the ubiquitous hydrocarbon contamination on van der Waals materials, Nat. Commun. **13**, 6770 (2022).

[26] Z. Li, Y. Wang, A. Kozbial, G. Shenoy, F. Zhou, R. McGinley, P. Ireland, B. Morganstein, A. Kunkel, S. P. Surwade, L. Li, and H. Liu, Effect of airborne contaminants on the wettability of supported graphene and graphite, Nat. Mater. **12**, 925 (2013).

[27] M. Campione, S. Trabattoni, and M. Moret, Nanoscale mapping of frictional anisotropy, Tribol. Lett. **45**, 219 (2012).

[28] See Supplemental Material at http://link.aps.org/supplemental/10.1103/PhysRevB.107.195442 for details of the 2DFF-AFM method, supplementary characterization results, further discussion of the model and the origins of isotropic and anisotropic friction components, and Refs. [35–49].

[29] Y. Guo, C. Liu, Q. Yin, C. Wei, S. Lin, T. B. Hoffman, Y. Zhao, J. H. Edgar, Q. Chen, S. P. Lau, J. Dai, H. Yao, H. S. P. Wong, and Y. Chai, Distinctive in-plane cleavage behaviors of two dimensional layered materials, ACS Nano **10**, 8980 (2016).

[30] M. Hirano, K. Shinjo, R. Kaneko, and Y. Murata, Anisotropy of Frictional Forces in Muscovite Mica, Phys. Rev. Lett. **67**, 2642 (1991).

[31] V. E. P. Claerbout, T. Polcar, and P. Nicolini, Superlubricity achieved for commensurate sliding: MoS_2 frictional anisotropy in silico, Comput. Mater. Sci. **163**, 17 (2019).

[32] P. Steiner, R. Roth, E. Gnecco, A. Baratoff, S. Maier, T. Glatzel, and E. Meyer, Two-dimensional simulation of superlubricity on NaCl and highly oriented pyrolytic graphite, Phys. Rev. B **79**, 045414 (2009).

[33] S. Morita, S. Fujisawa, and Y. Sugawara, Spatially quantized friction with a lattice periodicity, Surf. Sci. Rep. **23**, 1 (1996).

[34] O. E. Dagdeviren, Exploring load, velocity, and surface disorder dependence of friction with one-dimensional and two-dimensional models, Nanotechnology **29**, 315704 (2018).

[35] B. Schonfeld, J. J. Huang, and S. C. Moss, Anisotropic mean-square displacements (Msd) in single-crystals of 2h-MoS_2 and 3R-MoS_2, Acta Crystallogr. Sect. B **39**, 404 (1983).

[36] J. J. Cole, C. R. Barry, X. Wang, and H. O. Jacobs, Nanocontact electrification through forced delamination of dielectric interfaces, ACS Nano **4**, 7492 (2010).

[37] P. K. Chow, E. Singh, B. C. Viana, J. Gao, J. Luo, J. Li, Z. Lin, A. L. Elías, Y. Shi, Z. Wang, M. Terrones, and N. Koratkar, Wetting of mono and few-layered WS_2 and MoS_2 films supported on Si/SiO_2 substrates, ACS Nano **9**, 3023 (2015).

[38] A. Khajeh, Z. Chen, S. H. Kim, and A. Martini, Effect of ambient chemistry on friction at the basal plane of graphite, ACS Appl. Mater. Interfaces **11**, 40800 (2019).

[39] R. Addou, L. Colombo, and R. M. Wallace, Surface defects on natural MoS_2, ACS Appl. Mater. Interfaces **7**, 11921 (2015).

[40] H. Farahani, A. Rajabpour, M. Khanaki, and A. Reyhani, Interfacial thermal resistance between few-layer MoS_2 and silica substrates: A molecular dynamics study, Comput. Mater. Sci. **142**, 1 (2018).

[41] S. Munetoh, T. Motooka, K. Moriguchi, and A. Shintani, Interatomic potential for Si–O systems using Tersoff parameterization, Comput. Mater. Sci. **39**, 334 (2007).

[42] G. Will, M. Bellotto, W. Parrish, and M. Hart, Crystal-structures of quartz and magnesium germanate by profile analysis of synchrotron-radiation high-resolution powder data, J. Appl. Crystallogr. **21**, 182 (1988).

[43] J.-W. Jiang, H. S. Park, and T. Rabczuk, Molecular dynamics simulations of single-layer molybdenum disulphide (MoS_2): Stillinger-Weber parametrization, mechanical properties, and thermal conductivity, J. Appl. Phys. **114**, 064307 (2013).

[44] N. Onofrio, G. N. Venturini, and A. Strachan, Molecular dynamic simulation of tip-polymer interaction in tapping-mode atomic force microscopy, J. Appl. Phys. **114**, 094309 (2013).

[45] J. J. Cole, C. R. Barry, R. J. Knuesel, X. Wang, and H. O. Jacobs, Nanocontact electrification: Patterned surface charges affecting adhesion, transfer, and printing, Langmuir **27**, 7321 (2011).

[46] L. Liu, M. Qing, Y. Wang, and S. Chen, Defects in graphene: generation, healing, and their effects on the properties of graphene: A review, J. Mater. Sci. Technol. **31**, 599 (2015).

[47] Q. Li, T. E. Tullis, D. Goldsby, and R. W. Carpick, Frictional ageing from interfacial bonding and the origins of rate and state friction, Nature (London) **480**, 233 (2011).

[48] Z. Chen, A. Khajeh, A. Martini, and S. H. Kim, Chemical and physical origins of friction on surfaces with atomic steps, Sci. Adv. **5**, eaaw0513 (2019).

[49] K. Xu, P. Cao, and J. R. Heath, Graphene visualizes the first water adlayers on mica at ambient conditions, Science **329**, 1188 (2010).